High-Resolution Maps of Left Atrial Displacements and Strains Estimated With 3D Cine MRI Using Online Learning Neural Networks

Christoforos Galazis, Samuel Shepperd, Emma J. P. Brouwer, Sandro Queirós, Ebraham Alskaf, Mustafa Anjari, Amedeo Chiribiri, Jack Lee, Anil A. Bharath, and Marta Varela

***Abstract*—The functional analysis of the left atrium (LA) is important for evaluating cardiac health and understanding diseases like atrial fibrillation. Cine MRI is ideally placed for the detailed 3D characterization of LA motion and deformation but is lacking appropriate acquisition and analysis tools. Here, we propose tools for the Analysis of Left Atrial Displacements and DeformatIons using online learning neural Networks (Aladdin) and present a technical feasibility study on how Aladdin can characterize 3D LA function globally and regionally. Aladdin includes an online segmentation and image registration network, and a strain calculation pipeline tailored to the LA. We create maps of LA Displacement Vector Field (DVF) magnitude and LA principal strain values from images of 10 healthy volunteers and 8 patients with cardiovascular disease (CVD), of which 2 had large left ventricular ejection fraction (LVEF) impairment. We additionally create an atlas of these biomarkers using the data from the healthy volunteers. Results showed that Aladdin can accurately track the LA wall across the cardiac cycle and characterize its motion and deformation. Global LA function markers assessed with Aladdin agree well with estimates from 2D Cine MRI. A more marked active contraction phase was observed in the healthy cohort, while the CVD LVEF$_{\downarrow}$ group showed overall reduced LA function. Aladdin is uniquely able to identify LA regions with abnormal deformation metrics that may indicate focal pathology. We expect Aladdin to have important clinical applications as it can non-invasively characterize atrial pathophysiology. All source code and data are available at: https://github.com/cgalaz01/aladdin_cmr_la.**

***Index Terms*—Atrial cine MRI, left atrial function, segmentation neural network, image registration neural network, online learning, left atrial displacements, left atrial strains, atlas of the left atrium, left atrial mechanics.**

Received 16 September 2024; accepted 27 December 2024. Date of publication 6 January 2025; date of current version 2 May 2025. This work was supported in part by U.K. Research and Innovation (UKRI) Centres of Doctoral Training (CDT) in Artificial Intelligence for Healthcare (AI4H) (http://ai4health.io) under Grant EP/S023283/1; in part by St George's Hospital Charity; in part by the National Institute for Health and Care Research (NIHR) Imperial Biomedical Research Centre (BRC); and in part by the British Heart Foundation Centre of Research Excellence, Imperial College London, under Grant RE/18/4/34215. *(Corresponding author: Christoforos Galazis.)*

This work involved human subjects or animals in its research. Approval of all ethical and experimental procedures and protocols was granted by the North West-Preston Research Ethics Committee IRAS under Application No. 247295.

Christoforos Galazis is with the Department of Computing, Imperial College London, SW7 2AZ London, U.K. (e-mail: c.galazis20@imperial.ac.uk).

Samuel Shepperd was with the Department of Physics, Imperial College London, SW7 2AZ London, U.K. He resides in W12 0HZ London, U.K. (e-mail: samuel.shepperd19@imperial.ac.uk).

Emma J. P. Brouwer was with the Department of Physics, Imperial College London, SW7 2AZ London, U.K. She is now with the Spinoza Centre for Neuroimaging, 1105 BK Amsterdam, The Netherlands (e-mail: brouwer@herseninstituut.knaw.nl).

Sandro Queirós is with the Life & Health Sciences Research Institute (ICVS), School of Medicine, University of Minho, 4800-058 Braga, Portugal, and also with the ICVS/3B's—PT Government Associate Laboratory, 4710-057 Braga, Portugal (e-mail: sandroqueiros@med.uminho.pt).

Ebraham Alskaf, Amedeo Chiribiri, and Jack Lee are with the School of Biomedical Engineering & Imaging Sciences, King's College London, WC2R 2LS London, U.K. (e-mail: ebraham.alskaf@kcl.ac.uk; amedeo.chiribiri@kcl.ac.uk; jack.lee@kcl.ac.uk).

Mustafa Anjari is with the Department of Radiology, Royal Free Hospital, NW3 2QG London, U.K., also with the Department of Brain Repair and Rehabilitation, UCL Queen Square Institute of Neurology, WC1N 3BG London, U.K., and also with the Lysholm Department of Neuroradiology, National Hospital for Neurology and Neurosurgery, WC1N 3BG London, U.K. (e-mail: m.anjari@ucl.ac.uk).

Anil A. Bharath is with the Department of Bioengineering, Imperial College London, SW7 2AZ London, U.K., and also with Imperial Global Singapore, Singapore 138602 (e-mail: a.bharath@imperial.ac.uk).

Marta Varela is with the Cardiovascular and Genomics Research Institute, St George's University of London, SW17 0RE London, U.K., and also with the National Heart & Lung Institute, Imperial College London, SW7 2AZ London, U.K. (e-mail: mvarela@sgul.ac.uk).

Digital Object Identifier 10.1109/TMI.2025.3526364

I. Introduction

DISTURBANCES in atrial function are increasingly recognized as significant contributors to the development and progression of various cardiovascular diseases (CVDs), such as atrial fibrillation, atrial myopathy, heart failure, and stroke [1], [2], [3], [4], [5]. These atrial functional abnormalities are typically part of disease-induced remodelling processes [5], [6]. They can be accompanied by tissue-level changes, especially fibrotic remodelling or fatty deposition, and also organ-level remodelling, manifesting as changes in atrial size and shape. Organ-level remodelling is expected to be a later manifestation of CVD than changes at the cellular or tissue-level.

Current assessments of left atrial (LA) motion and deformation typically only capture global or one-dimensional changes in the atria. LA strains are usually estimated from single-plane long-axis echocardiograms [7] or magnetic resonance imaging (MRI) [8]. This is in contrast to the left ventricle (LV), for which several dedicated 3D regional metrics of motion and deformation exist [9], with known clinical correlates [10], [11], [12], [13]. This discrepancy highlights a lack of tools for a detailed 3D assessment of LA function and deformation. Here, we address this gap, introducing a novel end-to-end acquisition and image processing tool, Aladdin, that enables comprehensive 3D analysis of LA motion and deformation. We also present proof-of-concept analysis of LA function in 10 healthy volunteers and 8 CVD patients, to demonstrate Aladdin's future clinical potential.

A. LA Strains

The LA plays a vital role in cardiac function by modulating left ventricular filling and overall cardiac output. It operates through three phases: 1) reservoir phase, in which the LA is filled with oxygenated blood from the pulmonary veins, reaching its maximum volume; 2) conduit phase, where blood is passively emptied into the LV, reducing the LA volume; and 3) booster pump, in which the LA actively contracts, further emptying the chamber to its minimum volume [14]. Markers of LA motion and deformation, called "LA strains", are typically assessed across these phases using 2D cardiac long-axis through echocardiograms or dynamic (Cine) MRI [1], [15].

The global LA strain is a single value that describes the change in LA perimeter in a 4-chamber view [15]. It is the simplest and most reported strain value [15]. In 2D regional strain analysis, the change in length of specific segments of the LA contour is measured [15]. These LA strains, and their temporal derivatives, "LA strain rates", have been correlated with atrial fibrillation (AF) burden, heart failure (HF) burden, presence of LA fibrosis, heart valve disease and cardiomyopathies [2], [7], [16].

While these 2D LA strain markers are valuable, they have several limitations. As they are estimated from a single view, they suffer from sampling bias and characterize only 2D changes. Moreover, they provide an incomplete characterization of tissue deformations compared to the definition of strain in the physical sciences. In engineering, strains are tensors, which quantify the complex directional material deformations (3D stretches and shears) of a body in response to applied stresses. 3D full coverage strain measurements of the LA have the potential to capture vital information concerning tissue biomechanics, thereby expanding clinical applications [8]. These could include the identification of atrial regions of abnormally reduced strain, which could be associated with stiffer, fibrotic LA myocardium. Current LA fibrosis identification relies on late gadolinium-enhanced (LGE) MRI, a very subjective contrast agent technique with poor reproducibility [17], [18]. Furthermore, the use of LGE MRI carries the risk of gadolinium deposition, which can have adverse effects and may be contraindicated in certain patients [19]. Thus, there is a great need for better imaging tools for *in vivo* non-invasive LA tissue characterization.

As in the LV, regional strains may contribute to fibrosis identification [20]. Regional strain metrics are also likely to be early disease markers, preceding changes in global functional biomarkers such as ejection fraction [21]. Thus, high-resolution spatio-temporal 3D maps of LA deformation can potentially provide more specific, earlier signatures of CVD pathology that affects the atria, with enhanced diagnostic and prognostic value [19].

B. Cine MRI

Cine MRI is increasingly used to characterize LA motion, given its excellent signal-to-noise ratio, spatial resolution and operator-independence when compared to speckle tracking echocardiography (STE) [22], [23]. Cine MRI, which is widely included in clinical cardiac MRI examinations, allows the reconstruction of MR images at various cardiac phases, enabling a dynamic evaluation of cardiac motion. The LA is visible, although incompletely, in the 2-chamber, 4-chamber, and 3-chamber views, each acquired in a separate breath-hold as thick slices. These images have been used to study LA motion and deformation [1], [24], [25], usually analyzed using feature tracking (FT) techniques [1]. FT is a post-processing step [22] which involves the identification and tracking across the cardiac cycle of key features (e.g., manually or automatically delineated LA wall regions). These deformation analyses are inherently incomplete, as they are conducted as thick single-slice images that lack full LA coverage. Moreover, at the typical spatial resolution used for ventricular 2D Cine MR imaging (slice thickness: 8-10 mm, in-plane resolution: ~ 2 mm [26]), partial volume effects preclude an accurate identification and motion characterization of the LA wall. Different slices are also acquired at different breath-holds, further complicating 3D motion analysis. Nonetheless, 2D FT has been found clinically useful for the LA [27]. Previous studies have analysed LA function using stacks of thick slices covering the LA acquired in a short-axis view [28], [29] but 3D FT has not yet been explored due to the lack of 3D Cine MRI protocols for the LA.

C. Segmentation

Delineating (segmenting) the LA is critical for assessing its structure and function, particularly given its complex anatomy. Manual segmentation of the LA in 2D long-axis and short-axis Cine MRI demonstrates high agreement, with inter-observer intra-class correlation coefficient (ICC) ranging from 0.81 to 0.99 and intra-observer ICC ranging from 0.87 to 0.98 [30], [31], [32], [33]. Similarly, 3D LGE-MRI also shows strong observer agreement [34], with inter-observer ICC between 0.79 and 0.97 and intra-observer ICC between 0.95 and 0.98 [35].

Manual segmentation of medical images, which involves partitioning an image into anatomically meaningful regions, is an extremely repetitive and time-consuming process. Improved reproducibility and ease-of-use can be achieved through automated segmentation algorithms [31], which are predominately deep neural network (NN)-based. In cardiac MRI, U-Net [36] and its variants have been successfully deployed for LA segmentation of LGE-MRI [37], [38], [39], [40], [41]. More recently, nnU-Net [42] builds on the U-Net

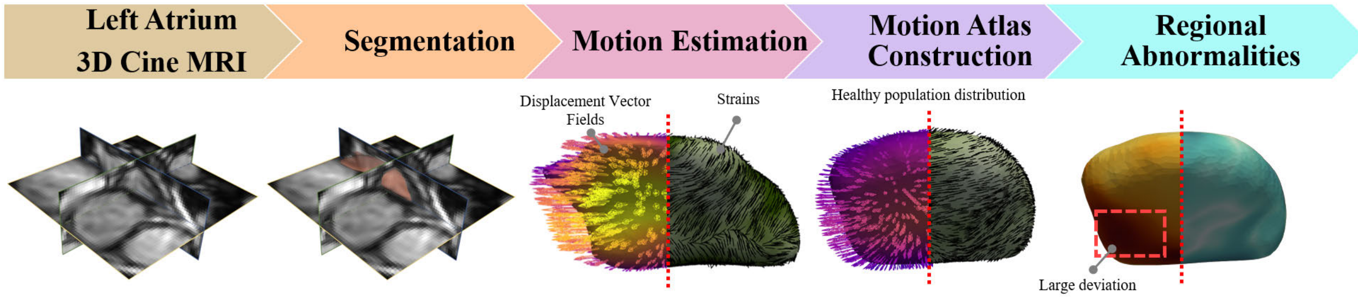

Fig. 1. Workflow of the Analysis for Left Atrial Displacements and Deformations using onlIne learning neural Networks, *Aladdin*: **(A)** Take as input a 3D high-resolution sequence of MR images of the left atrium (LA) and segmentation maps of 3 cardiac phases. **(B)** Predict segmentation of all cardiac phases using a segmentation network. **(C)** Predict the Displacement Vector Field (DVF) of the LA image contours across the cardiac cycle using an image registration network and calculate the surface principal strains. **(D)** Construct a displacement and strain LA atlas combining data from 10 healthy subjects. **(E)** Identify regional motion abnormalities by estimating the Mahalanobis distance between a given patient's data and the atlas distribution.

architecture and introduces an automated training pipeline including preprocessing and postprocessing steps, leading to impressive results on a variety of medical images, including cardiac MRI.

D. Displacement Vector Field

A necessary step for characterizing atrial deformations is the tracking of the position of regions of interest in the images across the cardiac cycle. From these, displacement vector fields (DVFs), the vectors that link material points in the myocardium across different phases of the cardiac cycle, can be estimated.

DVFs are usually computed by aligning (registering) images across the cardiac cycle, as we propose here, or by using optical flow techniques such as block matching [22]. Strain tensors can be estimated through mathematical manipulation of the DVFs.

NNs are increasingly used for image registration, offering advantages such as improved accuracy and scalability over traditional techniques, but they also face challenges like the need for large labeled datasets and potential issues with generalizability [43], [44], [45]. Recently, various NN-based image registration methods have been proposed to analyze LV deformations across the cardiac cycle from Cine MR images. Common architectures are based on: U-Net [46], [47], [48], [49], variational autoencoders [50], [51], [52], or Siamese NN [53], [54]. Usually, the displacement field is learned in an unsupervised way by using a spatial resampling module [55] that estimates the DVFs between pairs of NN-registered images.

Segmentation maps of cardiac structures have been used with cardiac motion tracking networks to improve their performance. Typically, this can be accomplished by incorporating the segmentation outputs as part of the input [50], constraining the DVFs so the transformed segmentation maps agree with the target segmentation [46], or integrating them into a joint segmentation-motion tracking task [47], [54].

Out-of-the-box techniques designed for the LV are therefore unlikely to succeed in the LA, as the LA noticeably differs from the LV. The LA has much thinner myocardial walls [56], [57], [58], a more irregular and complex morphology [56], [59], and high structural diversity between individuals [56]. We therefore propose a specific registration NN for the LA as part of the Aladdin tool.

E. Atlas

The clinical value of LA regional motion characterization hinges on the ability to identify regional LA motion abnormalities. For this, LA maps of reference values of regional LA deformation biomarkers (such as DVF magnitude or principal strain values) are needed. These LA maps can be constructed by building an LA atlas of motion biomarkers. In this context, an atlas is a statistical model that characterizes the features of a specific population [60].

An atlas is typically created using registration techniques to align multiple representations (e.g., segmentation maps) of a given organ across a specific population [47], [61], [62]. Regional biomarkers (such as LA displacements and strains) can be mapped onto the atlas common reference space, to enable direct statistical and visual analyses across subjects [61], [62]. Atlases serve as standardized references for analyzing and comparing imaging data, and can provide a method for comprehensive characterization of normal LA motion and deformation patterns [60], [62], [63]. Furthermore, they allow for the identification of regional differences in biomarkers between pathological cases and the healthy population [64].

F. Overview and Aims

We propose *Aladdin*, Analysis of Left Atrial Displacements and DeformatIons with neural Networks, to automatically characterize LA displacements and strains from high-resolution 3D Cine MRI. We conduct a technical feasibility study to characterize LA displacements and strains in small healthy and CVD patient cohorts. We also create the first atlas of regional LA displacements and deformations across the cardiac cycle. As shown in Figure 1, Aladdin includes:

1) An online learning segmentation NN, nnU-Net [42], for the semi-automatic segmentation of the LA across the cardiac cycle.

2) An online weakly supervised learning image registration NN, Aladdin-R, to automatically estimate LA DVFs across the cardiac cycle.
3) An algorithm to calculate regional LA strains across the cardiac cycle, which treats the LA myocardium as an infinitesimally thin 2D surface.
4) The construction of a LA DVF and strain atlas using data from 10 healthy volunteers.
5) Proof-of-principle characterization of regional LA strains of cardiovascular patients using the created atlas.

II. Methods

The source code for Aladdin, the atlas, as well as the anonymized Cine MR images, are publicly available: https://github.com/cgalaz01/aladdin_cmr_la and https://zenodo.org/records/13645121. Referenced supplementary material can be viewed at: https://github.com/cgalaz01/aladdin_cmr_la/tree/main/supplements.

A. LA Cine MR Images

We use 3D Cine MRI balanced Steady State Free Precession (bSSFP) scans of the LA acquired using a novel high-resolution acquisition protocol [65]. The images are electrocardiogram (ECG)-gated and acquired in a single 25-second breath-hold using a 1.5T Philips Ingenia MRI scanner with a 32-channel cardiac coil. The typical field of view used is 400 × 270 × 70 mm^3 and the acquisition matrix is 256 × 256 × 36 to give a reconstructed resolution of 1.72 × 1.72 × 2.00 mm^3. We use SENSE with factors of 2.3 and 2.6 along each phase encode direction, and 55% view sharing for a total of 20 phases across the cardiac cycle. Cardiac phase 0 corresponds to the ECG R-peak, representing ventricular end-diastole. This corresponds to atrial end-systole at which the LA is expected to have the smallest volume. An example cross-section of the 3D Cine images can be seen in Supplementary Figure (SupFig) 1 and slices across the cardiac cycle from two cases in SupVid 1 and 2.

We analyse images acquired after informed consent and under ethical approval from 18 subjects: 10 healthy volunteers (age: 30.4 ± 4.7 years; female: 40.0%), and 8 patients with cardiovascular disease (CVD) (age: 53.8 ± 15.7 years; female 62.5%). As this dataset was acquired to evaluate the clinical feasibility of the new LA protocol [65], patients do not necessarily have abnormal LA atrial function. The pathologies present in the CVD group are: myocarditis (1 patient), history of syncope (2), myocardial infarction (3), non-ischaemic cardiomyopathy (1), and hypertrophic cardiomyopathy (1). Two of these patients had a reduced LV ejection fraction ($\leq$40% [66]). Specifically, one with severe abnormality (22%) with confirmed diagnosis of myocardial infarction and the other with moderate abnormality (35%) with a diagnosis of hypertrophic cardiomyopathy and myocardial infarction. The remaining cases have either normal ($\geq$50%) or mild abnormality (40-49%). We therefore divide these two patients into a subgroup of "CVD LVEF$_\downarrow$" for further comparison.

To provide training and benchmarking data for Aladdin, the LA was manually segmented across the entire cardiac cycle for all subjects by two experts. The pulmonary veins (PV) and LA appendage (LAA) were excluded from the segmentation maps, as we focus on functional rather than structural variations in the atlas.

B. Preprocessing

The LA images are preprocessed to standardize their characteristics before being inputted to the NNs: they are cropped to a size of 96 × 96 × 36 voxels, centred at the LA, and their intensity is min-max normalized between [0, 1]. We also perform a rigid-body translation of the LA to ensure that its approximate centroid, estimated from the predicted segmentation maps, is stationary across the cardiac cycle.

C. nnU-Net: Segmentation Neural Network

To avoid manually segmenting the LA across all phases of the cardiac cycle, we use the state-of-the-art NN for medical image segmentation: nnU-Net [42]. Our implementation of the nnU-Net takes as input a 3D LA image in a given cardiac phase and predicts a corresponding LA binary segmentation map. We use the manual segmentation maps at the three cardiac phases (0, 8 and 15) as ground truth data for training. Given the limited availability of data, we adopt an online learning approach inspired by [53] and [67]. In this method, the model's weights are optimized solely using few unseen data from each new subject, starting from a randomly initialized state. This subject-by-subject training ensures that the model uniquely adapts to each individual. Subsequently, using the three manually segmented maps, we can predict the remaining LA segmentation maps for the subject.

D. Aladdin-R: Image Registration Neural Network

Aladdin-R is a 3D convolutional NN based on the U-Net architecture [36], implemented in TensorFlow [68]. As with U-Net, Aladdin-R uses encoding and decoding blocks to capture features at different spatial resolutions, and skip connections to preserve higher-resolution features. Rather than the standard skip connections between each encoder and decoder block we use squeeze and excitation (SE) blocks [69], which offer dynamic feature map-wise re-calibration, with a squeeze ratio of 8. The complete architecture can be seen in Figure 2.

As we are only interested in the motion of the LA wall, we use masked MR images of the LA myocardium (Figure 2 left panel) as inputs to the registration NN, Aladdin-R. This approach removes any irrelevant tissue to reduce tracking errors while leaving enough context for the network to distinguish between the LA wall and surrounding tissues. We first extract the contours of the LA segmentation maps yielded by nnU-Net across the cardiac cycle. The LA contours are then dilated using a spherical structure with a radius of 1 voxel. Using this dilated LA contour segmentation, the original LA images are masked out and used as inputs to Aladdin-R.

Aladdin-R takes in a pair of contour-masked 3D LA images from the same patient: one at phase 0 (moving image), and the other at another cardiac phase (target image). The outputs of the model are the deformed moving image and the associated DVFs that encode this non-linear transformation.

For Aladdin-R, the 3D input pairs are combined into a unified 3D image, each represented as a different channel.

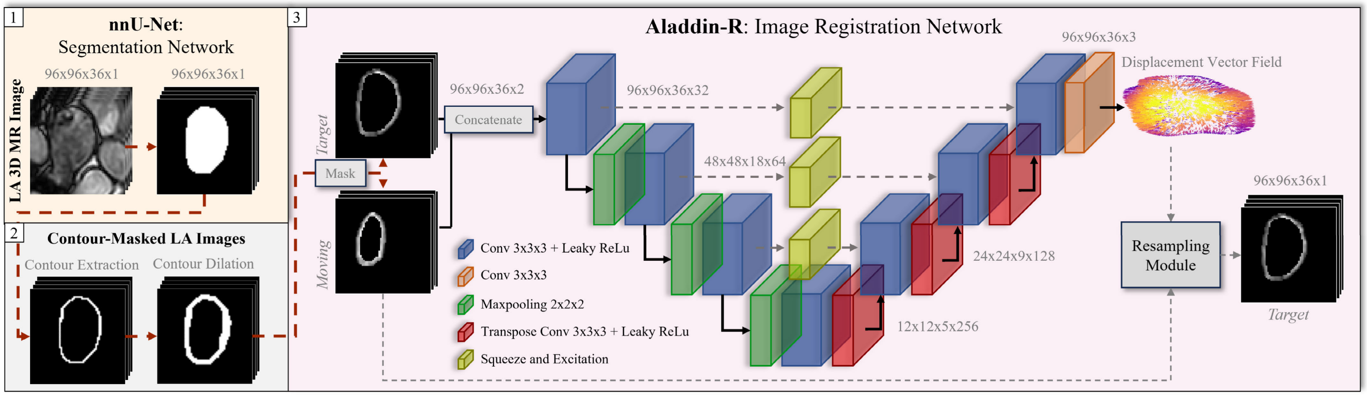

Fig. 2. Aladdin's image registration workflow. It consists of: **1)** an online learning (subject-by-subject basis) nnU-Net that estimates the LA segmentation maps, **2)** contours from the LA segmentation maps are first extracted and then dilated to create masks for the images, and **3)** an online learning 3D U-Net-like image registration network, Aladdin-R.

Aladdin-R's final convolutional layer uses a linear activation function and outputs each vector component of the DVF as a distinct feature map. This DVF is enforced through the usage of a 3D spatial resampling module [55], similarly to VoxelMorph [49], as a final layer. The resampling module linearly resamples the moving image to the target image given the predicted DVF.

We employ online learning to train Aladdin-R on all the cardiac phases from a single subject for 500 epochs. We use the Adam optimizer algorithm with parameters specified from [70]. The weights are updated by minimizing the mutual information loss [71] (the negative of the mutual information) between the target and the resampled moving image with an empirically set bin size of 128. The learning rate is set to 0.001, a learning decay rate of 0.8, and a batch size of 1.

The image registration task is ill-posed because the image similarity loss does not guarantee a unique optimal DVF solution. Moreover, the expected deformations of the LA across the cardiac cycle should be spatio-temporally smooth to preserve its physical integrity. For these reasons, we add a bending energy regularization term to the loss function [72], with an empirically selected regularization weight of 0.1. This regularizer will guide Aladdin-R towards a physiologically plausible solution.

E. LA Strain Calculation

Due to the LA's thinness relative to its other dimensions [73], we treat it as an infinitesimally thin surface [74]. Strains on each LA segment can therefore be represented by a 2D symmetric tensor with two principal strain directions (embedded on the surface LA mesh) and two corresponding principal strain values.

We first obtain a closed surface triangular mesh of the LA by applying the marching cubes algorithm to the LA segmentation from the first cardiac phase using scikit-image [75]. We then use the PyVista library [76] for the mesh smoothing.

For each triangular cell in the LA mesh, we calculate the finite Green-Lagrangian strain tensors [77] using cardiac phase 0 as the reference (undeformed) state. We take the following steps:

1) We calculate the metric tensor, g, of the vertex points in curvilinear coordinates. For each LA mesh triangle with vertex positions x_0, x_1 and x_2, defined in a Cartesian basis, the normalized covariant base $v = [g_1, g_2, g_3]$ can be calculated using:

$$
\begin{aligned}
g_1 &= \frac{x_1 - x_0}{||x_1 - x_0||}\\
g_2 &= \frac{x_2 - x_0}{||x_2 - x_0||}\\
g_3 &= g_1 \times g_2\\
g &= v^T \cdot v
\end{aligned}
\tag{1}
$$

2) The metric tensors at the reference configuration (cardiac phase 0), G_{ij}, and in each of the deformed configurations, g_{ij}, can be used to estimate the Green-Lagrange strain tensor E_{ij} [78, Chapter 5]:

$$
E_{ij} = \frac{1}{2}(g_{ij} - G_{ij}) \tag{2}
$$

3) E_{ij} are represented in local covariant coordinates, which are difficult to interpret. We now rewrite them in Cartesian coordinates for the reference configuration, E_{kl}, represented by the orthonormal basis (e_1, e_2, e_3):

$$
\begin{aligned}
e_1 &= g_1\\
e_2 &= \frac{g_2 - g_2 \cdot e_1}{||g_2 - g_2 \cdot e_1||}\\
e_3 &= \frac{e_1 \times e_2}{||e_1 \times e_2||}
\end{aligned}
\tag{3}
$$

4) The Green-Lagrangian strain tensor is calculated as:

$$
E_{kl} = E_{ij}(e_k \cdot G^i)(G^j \cdot e_l) \tag{4}
$$

5) We compute the eigenvalues (λ) and eigenvectors (v) of E defined in Step 4. As the LA is represented by a 2D surface, the strain eigenvalue corresponding to the direction orthogonal to the local LA surface is always 0. The principal strain value and direction of E at each triangular cell in the LA are treated as the regional main biomarkers of LA function.

F. LA Atlas Generation

We create an atlas of the LA with the segmentation maps from the 10 healthy volunteers, to allow the direct comparison and statistical analyses of the calculated DVF and strain metrics. To construct the atlas, we follow a similar strategy to the brain atlas creation steps detailed in [61] using the SimpleITK [79] package.

The first step consists of registering the LA segmentation in cardiac phase 0 of each case (i) to an arbitrary selected reference case, in a forward transformation (T_i) step. This consists of successive affine and non-rigid diffeomorphic registrations.

Then, to avoid biasing the atlas to the randomly selected reference case, we calculate the average inverse transformation ($\overline{T}^{-1}$): $\overline{T}^{-1} = \frac{1}{n}\sum_{i=1}^{n} T_i^{-1}$. This has proven to be a robust strategy in minimizing potential biases of the atlas towards the initial reference case [61].

By applying $T\overline{T}^{-1}$ to each i, we transform each case into the atlas space. We overlay these transformed cases to obtain the atlas consensus segmentation map which requires at least 50% agreement between all cases. Then, we obtain the mesh of the atlas segmentation map using marching cubes. Additionally, we apply $T\overline{T}^{-1}$ to the left and right PV, and LAA landmark points of each case. The average positions of these landmarks are used to indicate their locations on the atlas.

The final step consists of the registration of the DVF and strain fields estimated in each subject to the atlas space, using appropriate change of basis transforms.

We construct the final atlas by obtaining the mean, standard deviation and coefficients of variation (CV) of the motion and deformation metrics: magnitude of DVFs, principal strain directions and principal strain values. These are calculated at each LA atlas vertex, over all healthy subjects and across all cardiac phases.

As a potential tool to detect focal abnormalities in the LA, we can evaluate differences in regional LA function in a given subject in comparison to the healthy subjects' atlas. For this, we register that case directly to the atlas using the affine and non-rigid methods employed for atlas creation. Then, to quantify individual deviations from the atlas we use the Mahalanobis Distance (MD) [80]:

$$MD_{vt}(\mathbf{s_{vt}}) = \sqrt{(\mathbf{s_{vt}} - \boldsymbol{\mu_{vt}})^T \Sigma_{vt}^{-1} (\mathbf{s_{vt}} - \boldsymbol{\mu_{vt}})} \tag{5}$$

where $\mathbf{s}$ is the subject's metric, $\boldsymbol{\mu}$ is the atlas mean of the metric, $\boldsymbol{\Sigma}$ the atlas covariance, $\mathbf{v}$ indexes the vertex, $\mathbf{t}$ the cardiac phase.

G. Experimental Setup

We evaluate the models using the Hausdorff distance (HD, in mm) and Dice score (DS) metrics. HD measures the maximum distance between nearest points on the ground truth (GT) and predicted segmentation maps, with lower values indicating better performance. DS measures overlap, with 1 indicating perfect overlap. These analyses are performed across all phases of the cardiac cycle for each subject. We also measured inter-observer variability in 15 cases (7 healthy, 8 with CVD) and intra-observer variability in 6 cases (3 healthy, 3 with CVD) using the Dice score. Models were trained with three different random seeds, and results are presented as the average and standard deviation.

We compared Aladdin-R with state-of-the-art image registration methods: Advanced Normalization Tools (ANTs) [81], VoxelMorph (Vxm) [82], and VoxelMorph constrained on LA segmentation maps (Vxm-seg) [49]. The Medical Image Tracking Toolbox (MITT) [83], used in a similar study [65], is not applicable for contour images.

We also compared the estimated 3D strains from Aladdin-R with the global longitudinal strains (GLS) derived from the 2-chamber and 4-chamber views. The 2D strains are calculated as the Green-Lagrangian GLS, which represents the relative change in length of the LA perimeter [84]. This perimeter is measured by tracing the endocardial border of the LA throughout the cardiac cycle, excluding the mitral valve annulus, LAA, and PVs [85].

Furthermore, we evaluated the estimated LA ejection fraction (LAEF), defined as $(max\_volume - min\_volume)/max\_volume \times 100\%$, and LA active ejection fraction (LAaEF), defined as $(preactivation\_volume - min\_volume)/preactivation\_volume \times 100\%$, between the 3D and long-axis views.

The approximate LA volume from the 2D long-axis view is estimated using the formula [86]: $\frac{8}{3\times\pi} \times \frac{A^2}{L}$, where A represents the area of the LA in either the 2-chamber or 4-chamber view, and L is the length from the midpoint of the mitral annular plane to the back wall of the corresponding chamber. For improved estimation, the combined 2-chamber and 4-chamber and the formula is updated to [86]: $\frac{8}{3\times\pi} \times \frac{A_{2ch}\times A_{4ch}}{\min(L_{2ch}, L_{4ch})}$, where A_{2ch} and A_{4ch} are the areas of the 2-chamber and 4-chamber views, respectively, and $\min(L_{2ch}, L_{4ch})$ is the minimum length between the two views.

All networks were trained on a single Nvidia RTX 6000. For training and inference of one case, nnU-Net and Aladdin-R required approximately 1 hour, and 20 minutes, respectively. ANTs and the atlas construction and registration were executed on a 3XS Intel Core i7 (10700K, 3.8GHz, 8 Core). To construct the atlas on the 10 healthy cases required 2.5 hours, while registering an individual case to the atlas required 6 minutes.

III. Results

Our proposed method successfully estimated high-resolution LA displacement and strain maps across the cardiac cycle from all 18 subjects. We additionally created an atlas of LA motion and deformation biomarkers in healthy volunteers, and showed how it can help identify preliminary differences in these biomarkers in the CVD patients.

A. LA Segmentation

The online learning nnU-Net, with a total of 16.1M trainable parameters, demonstrates high accuracy in segmenting the LA throughout the cardiac cycle, despite learning from augmented segmentation maps from 3 cardiac phases only. In the

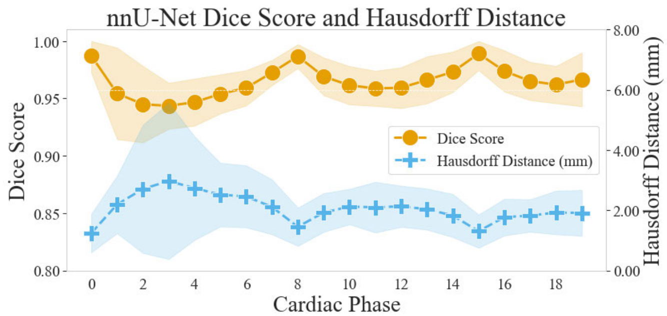

Fig. 3. The spatially averaged Dice score (orange line) and Hausdorff distance (mm) (blue dotted line) for the online learning nnU-Net across the cardiac cycle when trained on cardiac phases 0, 8, and 15 across all 18 subjects. The shaded areas around each line, colored to match the respective mean, indicate the standard deviation.

10 healthy cases, we achieve excellent HD of 2.42 ± 0.81 *mm* and DS of 0.97 ± 0.01. We observe similarly good results on the 8 CVD cases with a HD of 2.13 ± 1.15 *mm* and a DS of 0.97 ± 0.02. These values compare very well with the measured intra-observer and inter-observer agreement: DS of 0.96 ± 0.06 and 0.79 ± 0.16, respectively.

Although nnU-Net performs better on cardiac phases that are closer to the manual segmentation maps used for training (see Figure 3), our data augmentation scheme successfully prevents overfitting to the phases it was trained on. Representative segmentation results can be seen in Supplementary Videos (SupVid) 3 and 4.

B. LA Registration

Aladdin-R accurately tracks the LA wall across the cardiac cycle, including in cardiac phases with large displacements (see SupVid 5). When comparing the segmentation of the registered LA with the ground truth LA segmentation maps for the same cardiac phase, we obtain excellent HD of 1.14 ± 0.32 *mm* and DS of 0.98 ± 0.02.

The estimated DVF from Aladdin-R preserves the LA's expected rapid volume increase during the reservoir phase (0-8), followed by passive and active emptying during the conduit (9-15) and booster pump phases respectively (16-19). Aladdin-R consistently outperforms all other evaluated registration techniques in accuracy (see Table I) and spatio-temporal smoothness (see SupVid 6 and 7).

C. LA Deformation and Strains

When spatially averaged across the LA, the time course of the LA principal strain values closely tracks that of LA volume (see SupFig 2). The volume changes translate into clinically important global metrics such as the LAaEF and LAEF. Our 3D scans analysed with Aladdin lead to estimates of LAeEF and LAEF in good agreement with the traditional estimates from 2-chamber, 4-chamber, and 3D views - see Supplementary Table (SupTab) 1 and SupFig 3. 3D LAaEF has the highest Pearson correlation with the 4-chamber estimates, achieving a value of 0.83. In contrast, the 3D LAEF shows high correlation with estimates from all long-axis views, with a value of 0.93, 0.87, and 0.98, respectively for the 2-chamber,

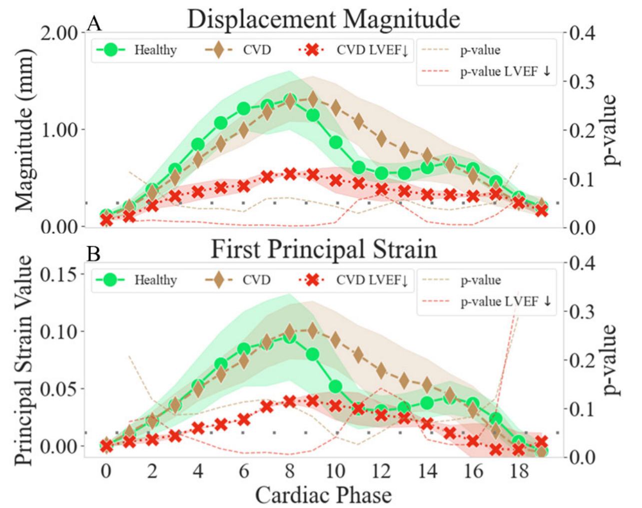

Fig. 4. Comparison between healthy (green), CVD (brown), and CVD LVEF$_\downarrow$ (red) groups across the cardiac cycle and their respective t-test *p*-values between healthy/CVD (dotted brown) and healthy/CVD LVEF$_\downarrow$ (dotted red). Plot *A* shows the DVF magnitude and plot *B* the first Green-Lagrangian principal strain values. The values shown are after registering each case to the atlas to reduce variance from LA size differences.

TABLE I
AVERAGE AND STANDARD DEVIATION OF IMAGE REGISTRATION RESULTS FOR THE LA CONTOUR MASK ACROSS THE CARDIAC CYCLE OVER THREE RUNS, ALONG WITH THE NUMBER OF TRAINABLE PARAMETERS FOR EACH IMAGE REGISTRATION MODEL

Model	Hausdorff Distance (mm)	Dice Score	#Params
ANTs	2.57 ± 1.37	0.72 ± 0.12	0
Vxm	4.70 ± 1.62	0.77 ± 0.09	2.8M
Vxm-seg	4.23 ± 1.86	0.72 ± 0.12	2.8M
Aladdin-R	$\mathbf{1.14 \pm 0.32}$	$\mathbf{0.98 \pm 0.02}$	2.2M

4-chamber, and 2/4-chamber. Additionally, we found that 3D LAaEF and LAEF correlate more strongly with LVEF than its 2D counterparts, with correlation values of 0.70 and 0.72, respectively.

The normalized mean principal strains measured using Aladdin and GLS estimates from the 2-chamber and 4-chamber views for the CVD cases are qualitatively similar in most cases - see SupFig 4. These GLS estimates are consistent with those reported in the literature [87], [88], [89], also taking into consideration the effects of aging [90]. Four cases, which include both CVD LVEF$_\downarrow$ cases, show noticeable discrepancies, primarily during the conduit and booster-pump phases, which are likely to come from the incomplete LA coverage provided by the long-axis analyses. Furthermore, the peak LA strains at the reservoir and conduit phases from the 2-chamber and 4-chamber views may occur at different cardiac phases. This variability is likely due to differences in the scanning planes and the irregular, complex structure of the LA.

When analysing 3D strains in more detail, we observed that the atria of the healthy and CVD groups undergo different deformations across the cardiac cycle, especially in the conduit and active phases (Figure 4). In the imaged cohorts, the

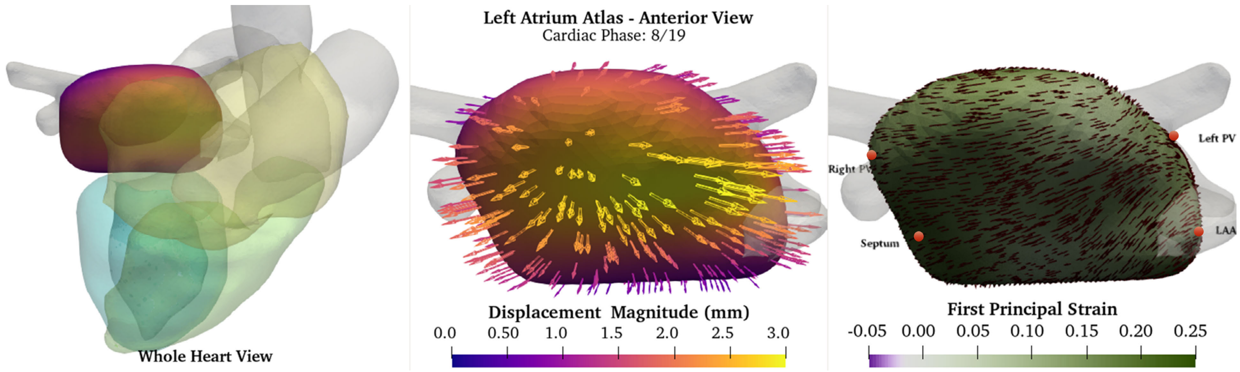

Fig. 5. **Atlas of the LA Displacements and Principal Strains:** From left to right: 1) Whole heart view with the LA atlas, 2) the generated DVF, and 3) the estimated first principal strains for the anterior view at the end-reservoir phase (phase 8). The atlas across the cardiac cycle can be viewed in SupVid 9.

atria of healthy subjects empty faster than that of the CVD patients leading to a more marked active contraction phase. This difference in deformation time course cannot be discerned using EF metrics. In contrast, CVD LVEF$_\downarrow$ cases showed a global decrease in LA function with low filling and slow emptying - see Figure 4).

Overall, the healthy cases had average DVF magnitudes of 0.67±0.40 mm and principal strain values of 0.04±0.04 across the whole cardiac cycle. The CVD cases had slightly higher averages of 0.71 ± 0.43 mm and 0.05 ± 0.04. Finally, the CVF LVEF$_\downarrow$ cases had much lower values of 0.34 ± 0.15 mm and 0.02 ± 0.02. The observed differences between the healthy and CVD cases are significant during the conduit phase (DVF: t-test $p < 0.05$; principal strain: t-test $p < 0.05$), while for CVD LVEF$_\downarrow$ cases, they are significant during the reservoir and booster-pump phases (DVF: t-test $p < 0.005$; principal strain: t-test $p < 0.05$).

Aladdin's main strength lies in its ability to provide otherwise unavailable insights into regional LA function and deformation, beyond global strain metrics. One of the findings from this feasibility study is that larger DVFs and principal strain values are observed at the anterior wall compared to other LA regions (see SupVid 8). In contrast, the smallest DVF and principal strain values can usually be found on the LA roof and posterior wall (see SupVid 8). The DVF and principal strain fields are spatially and temporally smooth, although the principal strain directions show a complex spatial alignment qualitatively consistent with LA myofibre orientations [91], [92].

D. LA Atlas

We were able to successfully register the LAs of all 10 healthy volunteers to a common space and calculate average DVF and strain biomarkers in this atlas. The resulting DVF and principal strain atlas can be seen in Figure 5 for the conduit phase and across the cardiac cycle in SupVid 9.

We obtained in the atlas an average (across space and time) DVF magnitude of 0.67 ± 0.39 and principal strain value of 0.04 ± 0.02. The atlas fields preserve the observed properties in the DVFs and strains, showing temporal and spatial smoothness and higher displacements on the anterior wall and very low displacements in the roof. The three phases of the LA (reservoir, conduit and booster pump) remain clearly distinct (see SupVid 9).

The atlas captures the normal values and ranges observed in the healthy cohort and allows regional assessments of individual cases. We assess this application of the atlas by identifying abnormal LA motion signatures on three patients with myocarditis, myocardial infarction (CVD LVEF$_\downarrow$ case) and non-ischaemic cardiomyopathy, respectively. The strain MD of these three cases can be seen in Figure 6 at the start of the boost-pump phase. During the boost-pump phase, the LA is actively contracting to empty blood, which provides an informative snapshot of its functional characteristics. Displacement and strain MD across the cardiac cycle for three representative healthy volunteers can be seen in SupVid 10, 11, and 12 and the three previously mentioned CVD cases can be seen in SupVid 13, 14 and 15, respectively. The regions with the most atypical deformation patterns correspond to the largest MD with respect to the healthy volunteer atlas. We observed that CVD cases generally have higher DVF MD and first principal strain MD on the anterior wall during the end of the reservoir and start of the booster-pump phases, compared to healthy cases. Additionally, CVD cases show higher MD values on the posterior wall (see SupVid 15) across the cardiac cycle. However, it is important to note that regions with small or no deformations, such as the posterior wall, may exhibit unreliable MD values because the mean coefficient of variation is close to 0. While the locations of large MD often overlap in the DVF and principal strain value maps, the DVF MD typically covers a larger region.

IV. Discussion

In this study, we present a novel non-invasive framework to study LA regional and global motion and strains, based on high-resolution 3D Cine MR images and comprehensive image analysis workflow, *Aladdin*. Aladdin consists of: a segmentation network, nnU-Net, to accurately identify the LA contours; an automatic image registration network to to extract LA DVFs, Aladdin-R; automatic strain tensor calculation from the DVFs; and, finally, the creation of a representative DVF and strain LA atlas. We show the feasibility of this approach by analysing images from 10 healthy volunteers and 8 patients

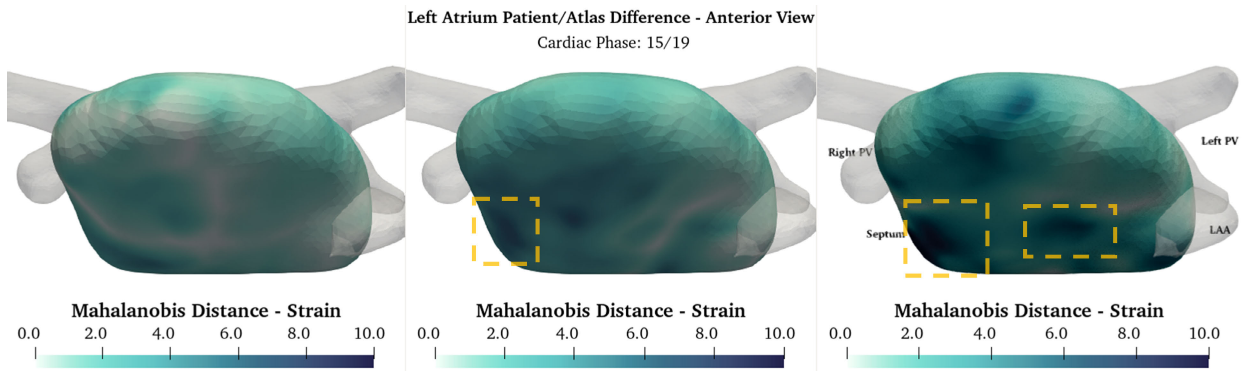

Fig. 6. Mahalanobis distance of the first principal strain between the atlas distribution and the estimates for three representative patients with, from left to right: myocarditis, myocardial infarction (CVD LVEF$_{\downarrow}$) and non-ischaemic cardiomyopathy. The anterior view at the start of the boost-pump phase is shown. Regions with a high Mahalanobis distance are highlighted with yellow boxes, which may indicate areas of regional functional abnormality.

with CVD and an indication for clinical MRI. Our technical feasibility results highlight the potential of this integrated methodology to provide clinicians and researchers with new regional biomarkers of LA motion and deformation.

A. Comparison With the Literature

As full-coverage Cine MRI of the LA is a new and emerging research field, there is limited previous work using this modality to compare to Aladdin. Varela and colleagues [73] obtained the 3D displacements from high-resolution 3D Cine using the MITT [83] on the LA segmentation maps. Morris et al, [93], on the other hand, focused on the identification of fibrotic tissue using full LA coverage MRI acquired using thick 2D slices. Displacements were estimated using ANTs [81]. In the current study, Aladdin-R led to more accurate DVF estimations than these methods or other existing conventional or data-driven methods - see SupVid 6 and 7.

Aladdin's LA motion and deformation measurements are in good general agreement with global long-axis Cine estimates and the literature from 2D STE. Specifically, highest strain values are achieved during the end of the reservoir phase and a smaller peak during the start of the booster-pump phase [94], [95]. Additionally, the largest motion is observed on the anterior rather than the posterior side of the LA wall, and smallest motion on the roof [96]. The principal strain directions are predominantly parallel to the mitral valve plane throughout the cardiac cycle [94], [95]. We speculate whether Aladdin may additionally contribute to the estimation of LA myocardial fibre directions, which are important determinants of atrial electrophysiology and biomechanics. In particular, it would be interesting to compare our imaging-based estimation of the principal strain directions during the active contraction phase with the LA fibre orientation directions proposed using other methods [91], [97], [98], [99].

As we use a novel high-resolution imaging protocol, we have a comparatively small dataset of 18 subjects, unsuitable for traditional deep learning techniques. Online learning, employed in both the supervised nnU-Net and the weakly supervised Aladdin-R, is a natural choice to overcome issues of limited data and effectively address the large (compared to LV) structural and functional variability of the LA. As the networks are optimized on a subject-by-subject basis, they reduce biases from the training data and can continue to be employed in future studies to analyse images from subjects with various clinical presentations. The proposed methods are also well suited for future analyses of the motion and deformation of the right atrium or right ventricle (which are often also approximated as thin surfaces).

In this study, we focus on DVFs and principal Green-Lagrangian strain values (with ventricular end-diastole as the Lagrangian reference frame) to characterize LA motion. Other related physical variables instead, such as strains in an Eulerian frame, the rate of change of the strain metrics [14], or projections of these variables into a cylindrical reference frame as often calculated in the LV [46], can all be easily computed from the metrics we present in this paper. Future studies should identify which biophysical variables are most useful in different clinical applications.

The proposed atlas allows rapid and reproducible assessments of LA DVF and/or strain irregularities, as manual comparison of 3D DVFs and strains is not only labour-intensive but also prone to errors. In the current study, we use the MD to identify regions of the LA with abnormal biomarkers. This identification is likely to be more robust when several deformation metrics (e.g., principal strain value and DVF magnitude) are considered simultaneously, as will be explored in future studies. This analysis can be performed using the proposed atlas or other techniques for analysing regional LA information, such as the universal atrial coordinate 3D LA surface mapping system [91].

Regional analyses of LA motion and deformation are likely to be clinically valuable for the identification of dense fibrosis or scar in the LA, as these regions are stiffer than healthy myocardium. Scar identification using LGE-MRI is generally reproducible, but quantifying diffuse myocardial fibrosis is highly subjective and less reproducible [17], [18].

B. Limitations and Future Work

In future iterations of Aladdin, the segmentation and image registration tasks could be joined, as they are closely intertwined. This could improve overall performance as has been shown for the LV [47]. Trained on image pairs to identify voxel displacement, Aladdin-R is agnostic to the cardiac phases provided and lacks temporal regularization. Although it already demonstrates strong temporal smoothness, its performance may be enhanced by tracking each voxel across all phases, similarly to [100]. Lastly, DVF and strain estimates could be further improved by using biomechanics-informed regularization [101], perhaps in a physics-informed NN setting [102], [103]. All these refinements should contribute towards a more reliable DVF and strain estimation with little overheads to the processing time.

We plan to make a more representative atlas by acquiring and registering additional images of healthy volunteers with varied backgrounds and ages to update the atlas. The current atlas of LA motion uses images from 10 subjects, acquired in a single scanner, from a narrow age range and limited ethnicities that are not representative of the general population. This age gap (healthy: 30.4 ± 4.7 vs CVD: 53.8 ± 15.7) can also impact our current analysis, as older subjects tend to have reduced global LA conduit function [104].

We will also obtain more images of CVD cases, specifically AF cases. This will allow us to clinically evaluate the atlas' ability to identify diseased-induced functional abnormalities and further explore the links between atrial regional strain dysfunction and fibrosis.

LGE-MRI is used for detecting fibrosis but is not widely used in the atria. Following further analyses, 3D Cine MRI could be an alternative or complementary technique to LGE-MRI to identify LA fibrosis. This could have important clinical applications in AF treatment stratification, the personalization of catheter ablations [104] and potentially early characterization of the AF risk phenotype [5].

As is typical of Cine MRI-based motion analysis, we are not tracking the displacement of material points and instead use image registration methods with regularization to determine the displacements of the LA wall. This is expected to have little impact on the motion analysis in most circumstances. It may however lead to inaccurate strain estimates in the presence of atrial devices, severe focal atrial pathology or in other circumstances in which the smoothness assumptions of the regularization techniques may be compromised.

V. Conclusion

We present a method to estimate 3D global and regional strains and displacements of the left atrium. Using high-resolution 3D Cine scans, we propose Aladdin, a tool to reliably provide 3D DVF and strain maps of the entire LA and map the information to a common atlas space. We expect this will allow the discovery of novel clinical prognostic and diagnostic biomarkers of LA function and improve our understanding of the atria's involvement in cardiovascular disease processes.

References

[1] O. A. Smiseth, T. Baron, P. N. Marino, T. H. Marwick, and F. A. Flachskampf, "Imaging of the left atrium: Pathophysiology insights and clinical utility," *Eur. Heart J.-Cardiovascular Imag.*, vol. 23, no. 1, pp. 2–13, Dec. 2021.

[2] B. D. Hoit, "Evaluation of left atrial function: Current status," *Struct. Heart*, vol. 1, nos. 3–4, pp. 109–120, Mar. 2017.

[3] G. G. Blume et al., "Left atrial function: Physiology, assessment, and clinical implications," *Eur. J. Echocardiography*, vol. 12, no. 6, pp. 421–430, Jun. 2011.

[4] K. Inoue, H. Kawakami, Y. Akazawa, H. Higashi, T. Higaki, and O. Yamaguchi, "Echocardiographic assessment of atrial function: From basic mechanics to specific cardiac diseases," *J. Cardiovascular Develop. Disease*, vol. 9, no. 3, p. 68, Feb. 2022.

[5] M. J. Shen, R. Arora, and J. Jalife, "Atrial myopathy," *JACC, Basic Transl. Sci.*, vol. 4, no. 5, pp. 640–654, 2019.

[6] F. Bisbal, A. Baranchuk, E. Braunwald, A. Bayés de Luna, and A. Bayés-Genís, "Atrial failure as a clinical entity: JACC review topic of the week," *J. Amer. College Cardiol.*, vol. 75, no. 2, pp. 222–232, 2020.

[7] S. Montserrat et al., "Left atrial deformation predicts success of first and second percutaneous atrial fibrillation ablation," *Heart Rhythm*, vol. 12, no. 1, pp. 11–18, Jan. 2015.

[8] D. C. Peters, J. Lamy, A. J. Sinusas, and L. A. Baldassarre, "Left atrial evaluation by cardiovascular magnetic resonance: Sensitive and unique biomarkers," *Eur. Heart J.-Cardiovascular Imag.*, vol. 23, no. 1, pp. 14–30, Dec. 2021.

[9] Y. Nabeshima, Y. Seo, and M. Takeuchi, "A review of current trends in three-dimensional analysis of left ventricular myocardial strain," *Cardiovascular Ultrasound*, vol. 18, no. 1, pp. 1–21, Dec. 2020.

[10] L. Xu et al., "Value of three-dimensional strain parameters for predicting left ventricular remodeling after ST-elevation myocardial infarction," *Int. J. Cardiovascular Imag.*, vol. 33, no. 5, pp. 663–673, May 2017.

[11] A. Sugano et al., "Value of 3-dimensional speckle tracking echocardiography in the prediction of microvascular obstruction and left ventricular remodeling in patients with ST-elevation myocardial infarction," *Circulat. J.*, vol. 81, no. 3, pp. 353–360, 2017.

[12] D. Hayat et al., "Comparison of real-time three-dimensional speckle tracking to magnetic resonance imaging in patients with coronary heart disease," *Amer. J. Cardiol.*, vol. 109, no. 2, pp. 180–186, Jan. 2012.

[13] D. Medvedofsky et al., "2D and 3D echocardiography-derived indices of left ventricular function and shape: Relationship with mortality," *JACC, Cardiovascular Imag.*, vol. 11, no. 11, pp. 1569–1579, 2018.

[14] B. D. Hoit, "Left atrial size and function: Role in prognosis," *J. Amer. College Cardiol.*, vol. 63, no. 6, pp. 493–505, 2014.

[15] L. P. Badano et al., "Standardization of left atrial, right ventricular, and right atrial deformation imaging using two-dimensional speckle tracking echocardiography: A consensus document of the EACVI/ASE/industry task force to standardize deformation imaging," *Eur. Heart J.-Cardiovascular Imag.*, vol. 19, no. 6, pp. 591–600, Jun. 2018.

[16] L. Thomas et al., "Evaluation of left atrial size and function: Relevance for clinical practice," *J. Amer. Soc. Echocardiography*, vol. 33, no. 8, pp. 934–952, Aug. 2020.

[17] H. Chubb et al., "The reproducibility of late gadolinium enhancement cardiovascular magnetic resonance imaging of post-ablation atrial scar: A cross-over study," *J. Cardiovascular Magn. Reson.*, vol. 20, no. 1, p. 21, Feb. 2018.

[18] A. S. Fahmy, E. J. Rowin, R. H. Chan, W. J. Manning, M. S. Maron, and R. Nezafat, "Improved quantification of myocardium scar in late gadolinium enhancement images: Deep learning based image fusion approach," *J. Magn. Reson. Imag.*, vol. 54, no. 1, pp. 303–312, Jul. 2021.

[19] T. J. Fraum, D. R. Ludwig, M. R. Bashir, and K. J. Fowler, "Gadolinium-based contrast agents: A comprehensive risk assessment," *J. Magn. Reson. Imag.*, vol. 46, no. 2, pp. 338–353, Aug. 2017.

[20] A. S. Lota et al., "Prognostic significance of nonischemic myocardial fibrosis in patients with normal LV volumes and ejection-fraction," *JACC, Cardiovascular Imag.*, vol. 14, no. 12, pp. 2353–2365, Dec. 2021.

[21] N. Duchateau, A. P. King, and M. De Craene, "Machine learning approaches for myocardial motion and deformation analysis," *Frontiers Cardiovascular Med.*, vol. 6, p. 190, Jan. 2020.

[22] A. Schuster, K. N. Hor, J. T. Kowallick, P. Beerbaum, and S. Kutty, "Cardiovascular magnetic resonance myocardial feature tracking: Concepts and clinical applications," *Circulat., Cardiovascular Imag.*, vol. 9, no. 4, 2016, Art. no. e004077.

[23] J.-U. Voigt and M. Cvijic, "2- and 3-Dimensional myocardial strain in cardiac health and disease," *JACC, Cardiovascular Imag.*, vol. 12, no. 9, pp. 1849–1863, Sep. 2019.

[24] M. Habibi et al., "Cardiac magnetic resonance–measured left atrial volume and function and incident atrial fibrillation: Results from MESA (multi-ethnic study of atherosclerosis)," *Circulat., Cardiovascular Imag.*, vol. 9, no. 8, Aug. 2016, Art. no. 004299.

[25] A. Schuster et al., "Left atrial function with MRI enables prediction of cardiovascular events after myocardial infarction: Insights from the AIDA STEMI and TATORT NSTEMI trials," *Radiology*, vol. 293, no. 2, pp. 292–302, Nov. 2019.

[26] C. M. Kramer, J. Barkhausen, C. Bucciarelli-Ducci, S. D. Flamm, R. J. Kim, and E. Nagel, "Standardized cardiovascular magnetic resonance imaging (CMR) protocols: 2020 update," *J. Cardiovascular Magn. Reson.*, vol. 22, no. 1, p. 17, Jan. 2020.

[27] J. Xu, W. Yang, S. Zhao, and M. Lu, "State-of-the-art myocardial strain by CMR feature tracking: Clinical applications and future perspectives," *Eur. Radiol.*, vol. 32, no. 8, pp. 5424–5435, Aug. 2022.

[28] A. P. Lourenço et al., "Left atrial ejection fraction estimation using SEGANet for fully automated segmentation of CINE MRI," in *Proc. Int. Workshop Stat. Atlases Comput. Models Heart*, Lima, Peru. Cham, Switzerland: Springer, 2020, pp. 137–145.

[29] F. Uslu and M. Varela, "SA-Net: A sequence aware network for the segmentation of the left atrium in cine MRI datasets," in *Proc. IEEE 18th Int. Symp. Biomed. Imag. (ISBI)*, Apr. 2021, pp. 766–769.

[30] A. Alfuhied et al., "Reproducibility of left atrial function using cardiac magnetic resonance imaging," *Eur. Radiol.*, vol. 31, no. 5, pp. 2788–2797, May 2021.

[31] R. A. Gonzales et al., "Automated left atrial time-resolved segmentation in MRI long-axis cine images using active contours," *BMC Med. Imag.*, vol. 21, no. 1, p. 101, Dec. 2021.

[32] L. Tondi et al., "The use of dedicated long-axis views focused on the left atrium improves the accuracy of left atrial volumes and emptying fraction measured by cardiovascular magnetic resonance," *J. Cardiovascular Magn. Reson.*, vol. 25, no. 1, p. 10, Feb. 2023.

[33] M. Zareian et al., "Left atrial structure and functional quantitation using cardiovascular magnetic resonance and multimodality tissue tracking: Validation and reproducibility assessment," *J. Cardiovascular Magn. Reson.*, vol. 17, no. 1, p. 52, Jan. 2015.

[34] L. Li, V. A. Zimmer, J. A. Schnabel, and X. Zhuang, "Medical image analysis on left atrial LGE MRI for atrial fibrillation studies: A review," *Med. Image Anal.*, vol. 77, Apr. 2022, Art. no. 102360.

[35] A. D. Mărgulescu et al., "Reproducibility and accuracy of late gadolinium enhancement cardiac magnetic resonance measurements for the detection of left atrial fibrosis in patients undergoing atrial fibrillation ablation procedures," *EP Europace*, vol. 21, no. 5, pp. 724–731, May 2019.

[36] O. Ronneberger, P. Fischer, and T. Brox, "U-Net: Convolutional networks for biomedical image segmentation," in *Proc. 18th Int. Conf. Med. Image Comput. Comput.-Assist. Intervent.*, vol. 9351. Cham, Switzerland: Springer, 2015, pp. 234–241.

[37] F. Uslu, M. Varela, G. Boniface, T. Mahenthran, H. Chubb, and A. A. Bharath, "LA-Net: A multi-task deep network for the segmentation of the left atrium," *IEEE Trans. Med. Imag.*, vol. 41, no. 2, pp. 456–464, Feb. 2022.

[38] Z. Xiong et al., "A global benchmark of algorithms for segmenting the left atrium from late gadolinium-enhanced cardiac magnetic resonance imaging," *Med. Image Anal.*, vol. 67, Jan. 2021, Art. no. 101832.

[39] A. Kausar, I. Razzak, M. I. Shapiai, and A. Beheshti, "3D shallow deep neural network for fast and precise segmentation of left atrium," *Multimedia Syst.*, vol. 29, no. 3, pp. 1739–1749, Jun. 2023.

[40] K. K. L. Wong, A. Zhang, K. Yang, S. Wu, and D. N. Ghista, "GCW-UNet segmentation of cardiac magnetic resonance images for evaluation of left atrial enlargement," *Comput. Methods Programs Biomed.*, vol. 221, Jun. 2022, Art. no. 106915.

[41] L. Li, V. A. Zimmer, J. A. Schnabel, and X. Zhuang, "AtrialJSQnet: A new framework for joint segmentation and quantification of left atrium and scars incorporating spatial and shape information," *Med. Image Anal.*, vol. 76, Feb. 2022, Art. no. 102303.

[42] F. Isensee, P. F. Jaeger, S. A. A. Kohl, J. Petersen, and K. H. Maier-Hein, "nnU-Net: A self-configuring method for deep learning-based biomedical image segmentation," *Nature Methods*, vol. 18, no. 2, pp. 203–211, Feb. 2021.

[43] G. Haskins, U. Kruger, and P. Yan, "Deep learning in medical image registration: A survey," *Mach. Vis. Appl.*, vol. 31, nos. 1–2, pp. 1–18, Feb. 2020.

[44] Y. Fu, Y. Lei, T. Wang, W. J. Curran, T. Liu, and X. Yang, "Deep learning in medical image registration: A review," *Phys. Med. Biol.*, vol. 65, no. 20, p. 20, 2020, Art. no. 20TR01.

[45] N. O'Mahony et al., "Deep learning vs. traditional computer vision," in *Proc. Adv. Comput. Vis. Conf. (CVC)*. Cham, Switzerland: Springer, 2020, pp. 128–144.

[46] M. A. Morales et al., "DeepStrain: A deep learning workflow for the automated characterization of cardiac mechanics," *Frontiers Cardiovascular Med.*, vol. 8, p. 1041, Sep. 2021.

[47] M. Sinclair et al., "Atlas-ISTN: Joint segmentation, registration and atlas construction with image-and-spatial transformer networks," *Med. Image Anal.*, vol. 78, May 2022, Art. no. 102383.

[48] X. Zhang, C. You, S. Ahn, J. Zhuang, L. Staib, and J. Duncan, "Learning correspondences of cardiac motion from images using biomechanics-informed modeling," in *Proc. Int. Workshop Stat. Atlases Comput. Models Heart*. Cham, Switzerland: Springer, Sep. 18, 2022, pp. 13–25.

[49] G. Balakrishnan, A. Zhao, M. R. Sabuncu, J. Guttag, and A. V. Dalca, "VoxelMorph: A learning framework for deformable medical image registration," *IEEE Trans. Med. Imag.*, vol. 38, no. 8, pp. 1788–1800, Aug. 2019.

[50] G. A. Bello et al., "Deep-learning cardiac motion analysis for human survival prediction," *Nature Mach. Intell.*, vol. 1, no. 2, pp. 95–104, Feb. 2019.

[51] C. Qin, S. Wang, C. Chen, W. Bai, and D. Rueckert, "Generative myocardial motion tracking via latent space exploration with biomechanics-informed prior," *Med. Image Anal.*, vol. 83, Jan. 2023, Art. no. 102682.

[52] J. Krebs, H. Delingette, B. Mailhé, N. Ayache, and T. Mansi, "Learning a probabilistic model for diffeomorphic registration," *IEEE Trans. Med. Imag.*, vol. 38, no. 9, pp. 2165–2176, Sep. 2019.

[53] H. Yu et al., "FOAL: Fast online adaptive learning for cardiac motion estimation," in *Proc. IEEE/CVF Conf. Comput. Vis. Pattern Recognit. (CVPR)*, Jun. 2020, pp. 4313–4323.

[54] C. Qin et al., "Joint learning of motion estimation and segmentation for cardiac MR image sequences," in *Proc. Int. Conf. Med. Image Comput. Comput.-Assist. Intervent.*, Granada, Spain. Cham, Switzerland: Springer, 2018, pp. 472–480.

[55] M. Jaderberg, K. Simonyan, A. Zisserman, and K. Kavukcuoglu, "Spatial transformer networks," in *Proc. Adv. Neural Inf. Process. Syst.*, vol. 28, Dec. 2015, pp. 2017–2025.

[56] S. Whiteman et al., "An anatomical review of the left atrium," *Transl. Res. Anatomy*, vol. 17, Nov. 2019, Art. no. 100052.

[57] M. Varela et al., "Novel MRI technique enables non-invasive measurement of atrial wall thickness," *IEEE Trans. Med. Imag.*, vol. 36, no. 8, pp. 1607–1614, Aug. 2017.

[58] J. Whitaker et al., "The role of myocardial wall thickness in atrial arrhythmogenesis," *Europace*, vol. 18, no. 12, pp. 1758–1772, 2016.

[59] S. Y. Ho, J. A. Cabrera, and D. Sanchez-Quintana, "Left atrial anatomy revisited," *Circulat., Arrhythmia Electrophysiol.*, vol. 5, no. 1, pp. 220–228, Feb. 2012.

[60] A. A. Young and A. F. Frangi, "Computational cardiac atlases: From patient to population and back," *Experim. Physiol.*, vol. 94, no. 5, pp. 578–596, May 2009.

[61] A. Ericsson, P. Aljabar, and D. Rueckert, "Construction of a patient-specific atlas of the brain: Application to normal aging," in *Proc. 5th IEEE Int. Symp. Biomed. Imag., Nano Macro*, May 2008, pp. 480–483.

[62] W. Bai et al., "A bi-ventricular cardiac atlas built from 1000+ high resolution MR images of healthy subjects and an analysis of shape and motion," *Med. Image Anal.*, vol. 26, no. 1, pp. 133–145, Dec. 2015.

[63] P. Medrano-Gracia et al., "Atlas-based analysis of cardiac shape and function: Correction of regional shape bias due to imaging protocol for population studies," *J. Cardiovascular Magn. Reson.*, vol. 15, no. 1, p. 80, Jan. 2013.

[64] K. Gilbert, C. Mauger, A. A. Young, and A. Suinesiaputra, "Artificial intelligence in cardiac imaging with statistical atlases of cardiac anatomy," *Frontiers Cardiovascular Med.*, vol. 7, p. 102, Jun. 2020.

[65] M. Varela et al., "Strain maps of the left atrium imaged with a novel high-resolution CINE MRI protocol," in *Proc. 42nd Annu. Int. Conf. IEEE Eng. Med. Biol. Soc. (EMBC)*, Jul. 2020, pp. 1178–1181.

[66] P. Ponikowski et al., "2016 ESC guidelines for the diagnosis and treatment of acute and chronic heart failure: The task force for the diagnosis and treatment of acute and chronic heart failure of the European Society of Cardiology (ESC) developed with the special contribution of the heart failure association (HFA) of the ESC," *Eur. Heart J.*, vol. 37, no. 27, pp. 2129–2200, Jul. 2016, doi: 10.1093/eurheartj/ehw128.

[67] C. Lei, Y. Xing, and Q. Chen, "Blind video temporal consistency via deep video prior," in *Proc. Adv. Neural Inf. Process. Syst.*, Jan. 2020, pp. 1083–1093.

[68] M. Abadi et al. (2015). *TensorFlow: Large-Scale Machine Learning on Heterogeneous Systems*. [Online]. Available: https://www.tensorflow.org/

[69] J. Hu, L. Shen, and G. Sun, "Squeeze-and-excitation networks," in *Proc. IEEE Conf. Comput. Vis. Pattern Recognit.*, Jul. 2018, pp. 7132–7141.

[70] D. P. Kingma and J. Ba, "Adam: A method for stochastic optimization," in *Proc. 3rd Int. Conf. Learn. Represent. (ICLR)*, San Diego, CA, USA, Y. Bengio and Y. LeCun, Eds., 2015, pp. 1–15. [Online]. Available: http://arxiv.org/abs/1412.6980

[71] M. Hoffmann, B. Billot, D. N. Greve, J. E. Iglesias, B. Fischl, and A. V. Dalca, "SynthMorph: Learning contrast-invariant registration without acquired images," *IEEE Trans. Med. Imag.*, vol. 41, no. 3, pp. 543–558, Mar. 2022.

[72] D. Rueckert, L. I. Sonoda, C. Hayes, D. L. G. Hill, M. O. Leach, and D. J. Hawkes, "Nonrigid registration using free-form deformations: Application to breast MR images," *IEEE Trans. Med. Imag.*, vol. 18, no. 8, pp. 712–721, Aug. 1999.

[73] M. Varela et al., "Novel computational analysis of left atrial anatomy improves prediction of atrial fibrillation recurrence after ablation," *Frontiers Physiol.*, vol. 8, p. 68, Feb. 2017.

[74] J. Kiendl, M.-C. Hsu, M. C. H. Wu, and A. Reali, "Isogeometric Kirchhoff–Love shell formulations for general hyperelastic materials," *Comput. Methods Appl. Mech. Eng.*, vol. 291, pp. 280–303, Jul. 2015.

[75] S. van der Walt et al., "Scikit-image: Image processing in Python," *PeerJ*, vol. 2, p. e453, Jun. 2014, doi: 10.7717/peerj.453.

[76] C. Sullivan and A. Kaszynski, "PyVista: 3D plotting and mesh analysis through a streamlined interface for the visualization toolkit (VTK)," *J. Open Source Softw.*, vol. 4, no. 37, p. 1450, May 2019, doi: 10.21105/joss.01450.

[77] E. R. McVeigh and C. Öztürk, "Imaging myocardial strain," *IEEE Signal Process. Mag.*, vol. 18, no. 6, pp. 44–56, Nov. 2001.

[78] A. Le Van, *Nonlinear Theory of Elastic Plates*. Amsterdam, The Netherlands: Elsevier, 2017.

[79] B. C. Lowekamp, D. T. Chen, L. Ibáñez, and D. Blezek, "The design of SimpleITK," *Frontiers Neuroinform.*, vol. 7, p. 45, Dec. 2013.

[80] R. De Maesschalck, D. Jouan-Rimbaud, and D. L. Massart, "The Mahalanobis distance," *Chemometrics Intell. Lab. Syst.*, vol. 50, no. 1, pp. 1–18, 2000.

[81] B. B. Avants, N. Tustison, and G. Song, "Advanced normalization tools (ANTS)," *Insight J.*, vol. 2, no. 365, pp. 1–35, 2009.

[82] G. Balakrishnan, A. Zhao, M. R. Sabuncu, A. V. Dalca, and J. Guttag, "An unsupervised learning model for deformable medical image registration," in *Proc. IEEE/CVF Conf. Comput. Vis. Pattern Recognit.*, Jun. 2018, pp. 9252–9260.

[83] S. Queirós, P. Morais, D. Barbosa, J. C. Fonseca, J. L. Vilaça, and J. D'Hooge, "MITT: Medical image tracking toolbox," *IEEE Trans. Med. Imag.*, vol. 37, no. 11, pp. 2547–2557, Nov. 2018.

[84] J. Buggey and B. D. Hoit, "Left atrial strain: Measurement and clinical application," *Current Opinion Cardiology*, vol. 33, no. 5, pp. 479–485, 2018.

[85] R. M. Lang et al., "Recommendations for cardiac chamber quantification by echocardiography in adults: An update from the American society of echocardiography and the European association of cardiovascular imaging," *Eur. Heart J. Cardiovascular Imag.*, vol. 16, no. 3, pp. 233–271, Mar. 2015.

[86] R. M. Lang et al., "Recommendations for chamber quantification: A report from the American society of echocardiography's guidelines and standards committee and the chamber quantification writing group, developed in conjunction with the European association of echocardiography, a branch of the European society of cardiology," *J. Amer. Soc. Echocardiography*, vol. 18, no. 12, pp. 1440–1463, Dec. 2005.

[87] G.-G. Mălăescu, O. Mirea, R. Capotă, A. M. Petrescu, J. Duchenne, and J.-U. Voigt, "Left atrial strain determinants during the cardiac phases," *JACC, Cardiovascular Imag.*, vol. 15, no. 3, pp. 381–391, Mar. 2022.

[88] G. C. H. Gan, A. Ferkh, A. Boyd, and L. Thomas, "Left atrial function: Evaluation by strain analysis," *Cardiovascular Diagnosis Therapy*, vol. 8, no. 1, pp. 29–46, Feb. 2018.

[89] J. Kim et al., "Left atrial strain impairment precedes geometric remodeling as a marker of post-myocardial infarction diastolic dysfunction," *JACC, Cardiovascular Imag.*, vol. 13, no. 10, pp. 2099–2113, Oct. 2020.

[90] A. C. Boyd, D. A. B. Richards, T. Marwick, and L. Thomas, "Atrial strain rate is a sensitive measure of alterations in atrial phasic function in healthy ageing," *Heart*, vol. 97, no. 18, pp. 1513–1519, Sep. 2011.

[91] C. H. Roney et al., "Universal atrial coordinates applied to visualisation, registration and construction of patient specific meshes," *Med. Image Anal.*, vol. 55, pp. 65–75, Jul. 2019.

[92] F. Pashakhanloo et al., "Myofiber architecture of the human atria as revealed by submillimeter diffusion tensor imaging," *Circulat., Arrhythmia Electrophysiol.*, vol. 9, no. 4, Apr. 2016, Art. no. 004133.

[93] A. Morris, E. Kholmovski, N. Marrouche, J. Cates, and S. Elhabian, "An image-based approach for 3D left atrium functional measurements," in *Proc. Comput. Cardiol.*, Sep. 2020, pp. 1–4.

[94] A. Nemes, Á. Kormányos, P. Domsik, A. Kalapos, C. Lengyel, and T. Forster, "Normal reference values of three-dimensional speckle-tracking echocardiography-derived left atrial strain parameters (results from the MAGYAR-healthy study)," *Int. J. Cardiovascular Imag.*, vol. 35, no. 6, pp. 991–998, Jun. 2019.

[95] L. Bao et al., "Left atrial morpho-functional remodeling in atrial fibrillation assessed by three dimensional speckle tracking echocardiography and its value in atrial fibrillation screening," *Cardiovascular Ultrasound*, vol. 20, no. 1, pp. 1–14, Dec. 2022.

[96] P. Kuklik et al., "Quantitative description of the 3D regional mechanics of the left atrium using cardiac magnetic resonance imaging," *Physiolog. Meas.*, vol. 35, no. 5, pp. 763–775, May 2014.

[97] M. Varela, J. Zhao, and O. Aslanidi, "Determination of atrial myofibre orientation using structure tensor analysis for biophysical modelling," in *Proc. 7th Int. Conf. Funct. Imag. Model. Heart*. Cham, Switzerland: Springer, Jan. 2013, pp. 425–432.

[98] M. Krueger et al., "Modeling atrial fiber orientation in patient-specific geometries: A semi-automatic rule-based approach," in *Proc. Int. Conf. Funct. Imag. Modeling Heart*, New York City, NY, USA. Cham, Switzerland: Springer, Jan. 2011, pp. 223–232.

[99] S. Ho, "Atrial structure and fibres: Morphologic bases of atrial conduction," *Cardiovascular Res.*, vol. 54, no. 2, pp. 325–336, May 2002.

[100] Q. Wang et al., "Tracking everything everywhere all at once," in *Proc. IEEE/CVF Int. Conf. Comput. Vis. (ICCV)*, Oct. 2023, pp. 19738–19749.

[101] C. Qin, S. Wang, C. Chen, H. Qiu, W. Bai, and D. Rueckert, "Biomechanics-informed neural networks for myocardial motion tracking in MRI," in *Proc. 23rd Int. Conf. Med. Image Comput. Comput.-Assist. Intervent. (MICCAI)*, Lima, Peru. Cham, Switzerland: Springer, Jan. 2020, pp. 296–306.

[102] C. Herrero Martin et al., "EP-PINNs: Cardiac electrophysiology characterisation using physics-informed neural networks," *Frontiers Cardiovascular Med.*, vol. 8, p. 2179, Feb. 2022.

[103] P. Arratia López, H. Mella, S. Uribe, D. E. Hurtado, and F. S. Costabal, "WarpPINN: Cine-MR image registration with physics-informed neural networks," *Med. Image Anal.*, vol. 89, Oct. 2023, Art. no. 102925.

[104] C. Sohns and N. F. Marrouche, "Atrial fibrillation and cardiac fibrosis," *Eur. Heart J.*, vol. 41, no. 10, pp. 1123–1131, Mar. 2020.